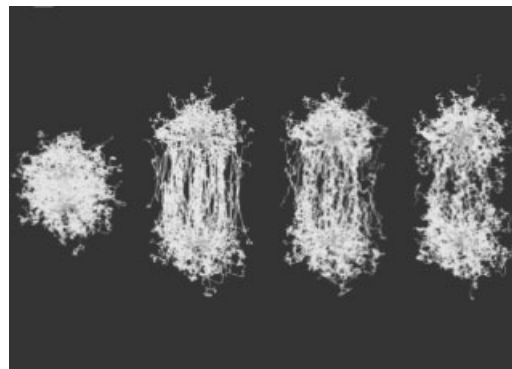


Coarse-Grained Simulations of Elongational Viscosities, Superposition Rheology and Shear Banding in Model Core–Shell Systems

A. van den Noort, W. J. Briels*

A recently developed coarse-grain model is used to investigate nonlinear rheological properties of model core–shell systems. The influence of several model parameters on the stresses and shear rates is investigated. Continuous planar elongational flow and superposition rheology are studied and compared to simple shear flow results. With particular values of the model parameters, an initially linear velocity profile splits into many bands with different shear rates and different densities, which finally merge into just two bands stacked along the gradient direction. With the box sizes used in our simulations, stick and Lees–Edwards boundary conditions lead to qualitatively similar results, with the stick boundary simulations showing better quantitative agreement with experiments.



Introduction

Most of the complex fluids have rheological properties which are interesting from an industrial application point view as well as from a theoretical point of view. While Newtonian liquids react to shear deformations by developing stresses proportional to the applied shear rates, complex fluids display a variety of more complex stress–rate of strain relationships. In many cases, the apparent viscosity, i.e. the ratio of stress and rate of strain decreases with the increase in shear rate, a phenomenon called shear thinning. In this paper, we perform simulations with a particular core–shell model exhibiting strong shear thinning and investigate some causes and consequences of the latter.

Usually, shear thinning in complex fluids is related to the process of perturbing and restoring some structural property characteristic of the quiescent state. Perturbations caused by an applied shear flow relax back to equilibrium with a characteristic time τ . At inverse shear rates larger than τ , relaxations are fast enough to keep the system effectively at equilibrium. At higher shear rates, the applied flow substantially changes the structure of the fluid and thereby its rheological properties. In the core–shell systems studied in this paper, this results in shear thinning. Other systems in which strong shear thinning occurs are solutions of rod-like colloids, worm-like micelles, polymer melts and polymer solutions.^[1–12] In the first two cases, it is believed that shear thinning results from alignment of the rods or worms caused by the flow. In the case of polymer melts, elongation of the polymer coils and subsequent alignment with the flow is believed to be the dominant mechanism for shear thinning. The same process may be responsible for shear thinning in polymer solutions. In this case, however, as opposed to polymer melts, large density fluctuations may occur, possibly leading to shear banding.

A. van den Noort, W. J. Briels
Computational Biophysics, Faculty of Science and Technology,
University of Twente, P.O. Box 217, 7500 AE Enschede,
The Netherlands
E-mail: w.j.briels@utwente.nl

In those cases where in the homogeneous state the stress as a function of shear rate reaches a plateau, or even decreases, the system becomes unstable and splits into two (or more) bands, stacked along the gradient direction and having different shear rates. This phenomenon is called shear banding.^[13] Several phenomenological theories have been developed to describe shear banding. Dhont has introduced the so called shear curvature contribution to the stress, and was able to describe shear banding at constant density.^[14] Olmsted and Fielding developed a theory in which the two bands are allowed to have different densities.^[15–19]

In this paper, we will extend the results published before.^[20,21] In the following section, we introduce our model and give some details of our simulations. In the next section, we investigate the relative importance of some model parameters. In the subsequent sections, we study elongational flow and superposition rheology, respectively. In the section Shear banding, we study some aspects of shear banding. Finally in the last section we summarize our findings.

It is perhaps interesting to note that banded structures also exist in sheared plastic materials.^[22] Although there are many similarities between the two types of banding, there are also important differences. We leave a detailed comparison for the future.

Model and Method

Model

The particles to be simulated are core–shell particles consisting of a central hard core covered with a corona of polymer chains. In our simulations, we coarse grained each particle to a single entity. In the coarse graining step, the average contributions of the coronas to the forces in the system become encoded in a very soft potential of mean force, which we will describe further on. In many cases of interest, however, it is important to realize that the instantaneous contributions of the coronas to the interactions between overlapping particles may well differ from the average values. When two particles are brought together to a distance r , the polymers in the coronas will start to interpenetrate and relax to some equilibrium state depending on the distance between the two particles. The polymers in the coronas form physicochemical connections, like for example, electrostatic or hydrogen bonds, or physical entanglements, collectively called ‘stickers’ from now on. Since the formation of these ‘stickers’ is equally slow as the movement of the centres of mass, they give rise to transient forces, which must be included in the model. To this end, we describe the state of overlapping coronas between particles i and j by a parameter n_{ij} , the number of stickers between i and j which in equilibrium has the value

$n_0(r_{ij})$. The equilibrium number of stickers is chosen to be $n_0(r) = 1 - [r_c/(r_c - \sigma)] [(r - \sigma)/r]$, which is unity at the diameter σ of the particles and zero at their cut-off distance $r_c = 4\sigma$, taken to be the diameter of the full particles including their coronas. We recently introduced a Brownian dynamics propagator which includes the effects of stickers:^[20]

$$\begin{aligned} d\mathbf{r}_i = & \langle \mathbf{V}(\mathbf{r}_i) \rangle dt + \nabla_i (kT/\xi_i) dt + \theta \sqrt{2kTdt}/\xi_i \\ & + \frac{1}{\xi_i} \sum_j \left\{ -\nabla_i \phi(r_{ij}) + \alpha [n_{ij} - n_0(r_{ij})] \frac{dn_0}{dr_{ij}} \frac{\mathbf{r}_{ij}}{r_{ij}} \right\} dt \end{aligned} \quad (1)$$

Here, $\langle \mathbf{V}(\mathbf{r}_i) \rangle$ is the average flow field at position \mathbf{r}_i and θ is a random number with zero mean and variance unity. The friction of particle i , ξ_i , consists of two contributions and quantifies the particle’s friction relative to the average flow field. The first contribution is the friction with respect to the solvent, the second describes the friction between neighbouring particles. The latter, for each partner j , is proportional to the number of stickers between i and j , if it is positive, and zero otherwise. ξ_i may, therefore, be written as

$$\xi_i = \xi_0 + \frac{1}{2} \xi_s \sum_j (n_{ij} + |n_{ij}|) n_0(r_{ij}) \quad (2)$$

The factor $n_0(r_{ij})$ has been added to make sure that the friction decays smoothly to zero for neighbouring particles beyond the cut-off distance r_c . We call ξ_s the friction per sticker. The friction per particle occurs in Equation (1) in a drift term, a random displacement and in front of the contribution of the forces to the displacement. The latter consist of two contributions, one being the thermodynamic forces originating from the effective potential $\phi(r_{ij})$, the other being the transient forces due to the corona–corona interactions. The effective thermodynamic particle–particle potential $\phi(r)$ is chosen as $\phi(r) = 4\epsilon (b/r)^8$, representing both the steep core–core potential and the weak corona–corona potential of mean force. The rather small range of the pair potential $\phi(r)$ compared to r_c reflexes the fact that at equilibrium, the coronas hardly influence each other at distances beyond about 2σ . This does not hold true for the sticker forces, which may be substantially different from zero even at separations slightly below r_c . As long as the number of stickers of two approaching particles is smaller than its equilibrium value $n_0(r_{ij})$, the two coronas will push each other resulting in a repulsion $\alpha [n_{ij} - n_0(r_{ij})] \frac{dn_0}{dr_{ij}}$ directed along $\mathbf{r}_{ij} = \mathbf{r}_i - \mathbf{r}_j$. On the other hand, when two particles in equilibrium are displaced to a larger separation, each corona will pull the other, resulting in an attraction between the particles. That is, two entangled coronas resist displacements in the direction of increasing absolute

values of $n_{ij} - n_0(r_{ij})$. With this role of $n_0(r_{ij})$ in mind, it is easy to understand that its range must be substantially larger than that of $\phi(r_{ij})$. Even when the more dilute parts of two coronas are brought into contact this temporarily leads to strong repulsions, which, however, finally relax to very small values.

The time evolution of the number of stickers is given by

$$dn_{ij} = -\frac{1}{\tau} [n_{ij} - n_0(r_{ij})] dt + \theta' \sqrt{\frac{2kT dt}{\alpha\tau}} \quad (3)$$

with θ' a random number with zero mean and unit variance. Here, we identify $1/\tau$ as the characteristic rate with which the sticker number strives towards its equilibrium value $n_0(r_{ij})$ for $r_{ij} < r_c$ or zero for $r_{ij} \geq r_c$. The second term on the right-hand side gives rise to random fluctuations of the sticker numbers. Since for pairs which are separated by a distance larger than r_c , we do not need to know n_{ij} and since for these values of r_{ij} they are doing no more than fluctuate around zero, we only keep track of n_{ij} for those pairs which are separated by a distance r_{ij} smaller than some value r_v , slightly larger than r_c , $r_v = 1.0625r_c$. When a particular pair enters this region, its sticker number n_{ij} is initialized according to the probability density $\propto \exp\{-1/2\beta\alpha n_{ij}^2\}$. Without this simplification, the simulation would hardly be feasible, because in that case all pairs should be considered in the simulation.

Having described the model and its implementation, let us clarify some of the motivations behind the particular choices that we made. First, Equation (1) and Equation (3) together give rise to an equilibrium distribution for the positions of the particles and the sticker numbers identical to the one obtained by integrating Equation (A1) over all particle and sticker velocities. The precise definition of the friction is irrelevant for this. We next calculate the probability distribution of the particle coordinates by integrating over all sticker numbers. Accepting negative values for the sticker numbers the resulting probability distribution of the particle coordinates is independent of $n_0(r_{ij})$ and simply proportional to $\exp(-\beta \sum_{(ij)} \phi(r_{ij}))$. This means that we can steer the thermodynamics of the system by the choice of the potential of mean force without bothering about the possible influences of the sticker forces. In practice, negative values of sticker numbers only occur near the cut off radius, where they give rise to fluctuating forces, as they should. Next, as already mentioned, the precise dependence of the friction on the sticker numbers does not influence the distribution of the coordinates, and may be chosen according to appropriate criteria. The choice made in Equation (3) meets the obviously necessary criterion that the friction should never be negative.

In Appendix A, we propose a second order version of this model. We describe the necessary ingredients and show

that the second order model gives in principle the same results as our present first order model.

Simulation Details

Our model may be mapped on different experimental systems, depending on the values of the parameters of the model. It is, therefore, useful to write all the results in terms of a set of characteristic variables of the model. These variables are chosen to be $1k_B T$ for energies, 1σ for distances and 1τ for time. The unit of length, σ , is defined as the distance r where the potential $\phi(r)$ reaches unity; it coincides with the point where the radial distribution function becomes unity for the first time, indicating that unit of length may be interpreted the hard-core diameter of the core-shell particles.

In all our calculations, we have used the parameters given in reduced units in Table 1, unless stated otherwise.

Except when stated differently, simulation boxes were cubic containing some 2 000–4 000 particles. Equilibrium simulations were done using periodic boundary conditions, while nonequilibrium simulations were done using Lees–Edwards boundary conditions^[23] to impose a flow in the x -direction with a velocity gradient $\dot{\gamma}$ in the y -direction. Average velocities were measured at different y -positions in the simulation box from the displacement of the particles. In order to reduce the noise in the instantaneous velocity field, we averaged it over its history with a weight function exponentially decaying in the past using a time constant $\tau_{\text{flow}} = 1000dt$. The local velocity of a given particle, to be used in the equations of motion [Equation (1)], was interpolated from the values in the nearest bins. In a similar way, average frictions were measured at different y -positions. The gradient of $\nabla_i(kT/\xi_i)$ was assumed to point along the y -axis; its value was calculated by comparing kT/ξ_i at neighbouring y -values. Stresses were calculated as $\mathbf{S} = 1/V \sum \mathbf{r}_i \mathbf{F}_i$ with \mathbf{F}_i the total force on particle i , i.e. the sum between curly brackets in the first

Table 1. Simulation parameters.

Parameter	Value	Unit
T	300	K
ρ	0.4	σ^{-3}
ϵ	240	$k_B T$
b	0.42	σ
α	0.473	$k_B T$
$\xi_0/\rho k_B T$	0.302	$\sigma\tau$
$\xi_s/\rho k_B T$	1.181	$\sigma\tau$
dt	5×10^{-5}	τ
r_c	4	σ

line of Equation (1) and V the volume of the box. Viscosities then followed from $\eta = S_{xy}/\dot{\gamma}$.

In the section Shear banding, we impose stick boundary conditions by applying a bounce-back rule for the particles colliding with the top and bottom of the box. We keep the bottom stationary and move the top according to the imposed shear rate. With every particle that tends to cross the wall, we calculate the exact fraction t_{coll} of the time step that has been consumed when the collision occurs. The new position of particle i is then set to:

$$\mathbf{r}(t + dt) = \mathbf{r}(t) + t_{\text{coll}}\mathbf{dr} + (1 - t_{\text{coll}}) \times (-\mathbf{dr} + 2\dot{\gamma}L_y dt \mathbf{e}_x) \quad (4)$$

where \mathbf{dr} is the displacement computed from Equation (1). The first two terms on the RHS of Equation (4) give the position of impact with the wall. The last term accounts for the bounce-back displacement for the remainder part of the time step and for an extra displacement in the flow direction from the moving wall, which is only added for collisions with the top wall.

Investigation of Some Model Parameters

In this section, we will investigate the relative importance of the various forces operating in our model as well as some other model parameters like the density of hard material.

Sticker Forces

In Figure 1, we have plotted viscosities as a function of shear rate for various values of α and all other parameters as given in Table 1. At small shear rates, the viscosities are seen to grow almost linearly with α . This is just an indication that sticker forces are dominant in this regime. At these low values of $\dot{\gamma}$, sticker numbers are close to their equilibrium values. Any movement of the centres of mass leads to deviations from the (new) equilibrium number of stickers, and hence to strong restoring forces. As a consequence, large shear forces are needed to deform and make flow the system.

With increasing shear rates, the above effect becomes less important. As soon as $\dot{\gamma}$ is equal to about $1/\tau$, two particles displaced along the gradient direction pass each other too fast for any substantial number of stickers to develop. Although the contribution of the sticker forces to the stress will be large, it is also independent of the shear rate. This contribution to the viscosity will, therefore, be proportional to $\dot{\gamma}^{-1}$. This is clearly observed in the figure. One more interesting aspect of Figure 1 is worthy to be mentioned. At the very high shear rates of about $50\tau^{-1}$,

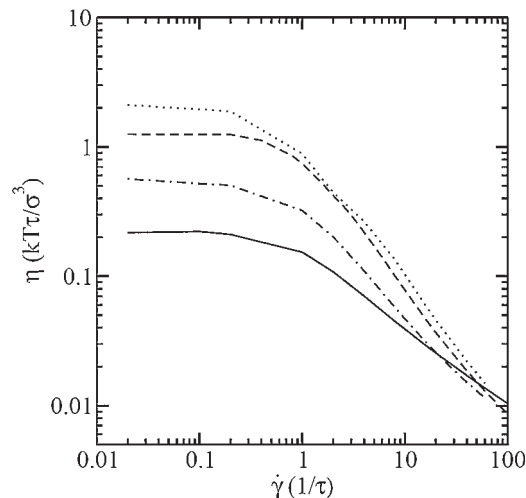


Figure 1. Shear viscosity η as a function of shear rate at different sticker force strengths α ; α is respectively $0.47k_B T$ (solid line), $1.89k_B T$ (dot-dashed line), $5.10k_B T$ (dashed line) and $8.32k_B T$ (dotted line).

the order of the curves inverts. While below this shear rate viscosities increase with increase in α , above it viscosities decrease with increase in α . This suggests that the stress, which is generated by the thermodynamic forces, is not independent of α , and in fact must decrease with increase in α . This is indeed confirmed in Figure 2, where we have plotted these contributions to the stress as a function of $\dot{\gamma}$ for several values of α . Over the entire range of shear rates, except for very small ones, the stresses resulting from the thermodynamic forces decrease proportional to α . The reason for this peculiar effect is the fact that with increase in shear rates the particles increasingly arrange in (structureless) layers in an effort to make the separation between the particles along the gradient direction as large

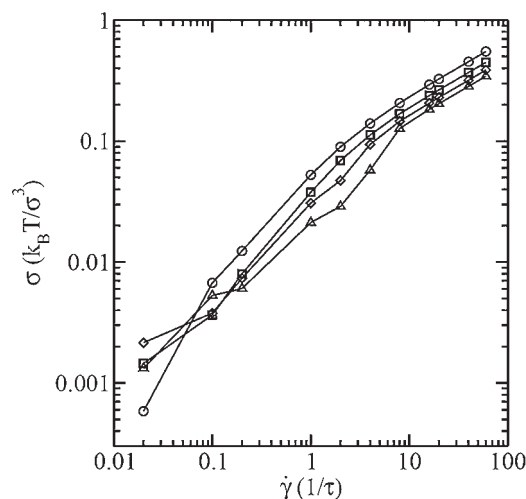


Figure 2. Conservative contribution to the stress tensor plotted versus the shear rate for values of α equal to $1.89k_B T$ (circle), $3.78k_B T$ (box), $5.67k_B T$ (diamond) and $7.56k_B T$ (triangle).

as possible, in order to diminish the forces even more. The larger the value of α , the larger the distance between these layers will be, and the smaller the contributions of the thermodynamic forces to the stress will be.

Obviously, the effect just mentioned should not occur at equilibrium and consequently not at small values of $\dot{\gamma}$. Indeed it is seen in Figure 2 that at shear rates below $0.05\tau^{-1}$ the order of the curves is the reverse of that at higher shear rates. Since it is rather difficult to obtain good statistics with nonequilibrium simulations at these low shear rates, we have calculated the time autocorrelation function of the contributions of the thermodynamic forces to the stress, and plotted the results in Figure 3. At $t = 0$ all curves have the same value, indicating that sticker forces do not influence static properties. The subsequent decay of these functions with time is seen to be slower with increasing values of α . Consequently, the integral of $G(t)$ from zero to infinity, i.e. the contribution of the thermodynamic forces to the viscosity, increases with increase in α .

It is perhaps interesting to notice that a similar crossover as the one just mentioned has been found in simulations of polymer melt rheology by means of FENE chains.^[24] In this case, zero shear viscosities increase with increase in chain length, while at the same time the degree of shear thinning increases to such an extent that at large shear rates viscosities decrease with increase in chain length. Although increase in α implies an increase in the influence of entanglements, it is not entirely equivalent to the increase in chain length, since in the latter case also τ and the friction change. The similarity of both phenomena remains striking however.

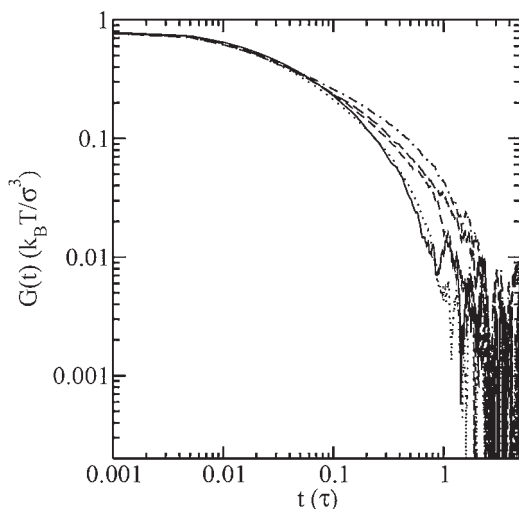


Figure 3. Stress autocorrelation at zero shear with only conservative forces included in the calculation of the stress tensor, for values of α equal to $1.89k_B T$ (solid line), $3.78k_B T$ (dotted line), $5.67k_B T$ (dashed line), $7.56k_B T$ (long dashed line) and $8.51k_B T$ (dot-dashed line).

Friction Per Sticker

In Figure 4, we have plotted viscosities as a function of $\dot{\gamma}$ for various values of the friction per sticker ξ_s . At low shear rates, viscosities increase almost linearly with ξ_s . This may be understood by noticing that at equilibrium the system samples experience stress in some order independent of friction, but they do so with a speed which is inversely proportional to ξ . As a consequence, all stress–stress autocorrelation functions $G_\xi(t)$ are roughly the same except for a scaling of the time axis by the friction: $G_\xi(t) = G_{\xi_0}(t\xi_0/\xi)$. Consequently, the viscosity being the integral of $G_\xi(t)$ from zero to infinity, is roughly proportional to ξ , i.e. roughly proportional to ξ_s . In the case of a nonequilibrium simulation, the deformation of the path followed by the system at a shear rate $\dot{\gamma}$ and friction ξ is similar to that at a shear rate $\dot{\gamma}\xi/\xi_0$ and friction ξ_0 . A time average of the stress will yield the same result in both cases, leading to viscosities proportional to ξ . This proportionality of the viscosity with ξ and hence roughly with ξ_s is seen to hold over the entire range of shear rates presented in Figure 4. In Figure 5, we plot similar curves for a system with number density $\rho = 0.1\sigma^{-3}$ and $\alpha = 9.5k_B T$. Again, at low shear rates viscosities are roughly proportional to ξ_s , but at high shear rates this is not true anymore. We will discuss this system further in the section Shear banding.

Elongational Viscosities

In a previous paper,^[20] we calculated the flow curve, i.e. shear viscosities versus shear rates, of our present model for the specifications given in Table 1. The results exhibit a strong shear thinning at shear rates around $1/\tau$. Roughly speaking, shear thinning occurs because the contributions

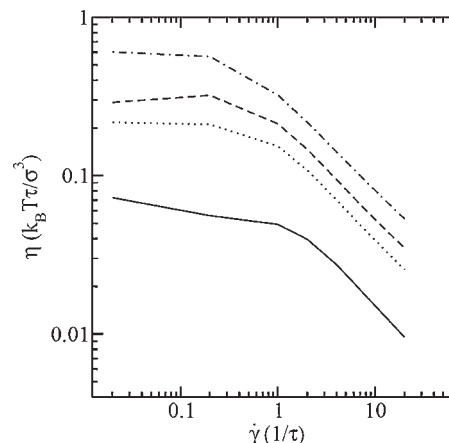


Figure 4. Viscosity versus shear rate for different values of the friction per sticker ξ_s , at $\varphi = 0.21$ and $\alpha = 0.47k_B T$. The lines represent respectively $\xi_s/\rho k_B T = 0.12\sigma\tau$ (solid), $1.18\sigma\tau$ (dotted), $2.36\sigma\tau$ (dashed) and $5.90\sigma\tau$ (dot-dashed).

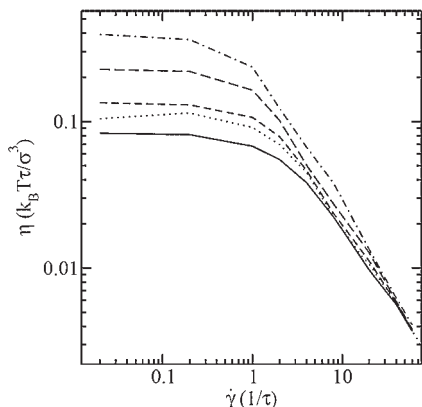


Figure 5. Viscosity versus shear rate for different values of the friction per sticker ξ_s , with $\varphi = 0.10$ and $\alpha = 9.5k_B T$. The lines represent respectively $\xi_s / \rho k_B T = 0.09\sigma\tau$ (solid), $0.19\sigma\tau$ (dotted), $0.27\sigma\tau$ (dashed), $0.79\sigma\tau$ (long dashed) and $2.36\sigma\tau$ (dot-dashed).

of the sticker forces to the stress become 'saturated' at high shear rates. The idea is that two particles, displaced with respect to each other along the gradient direction, are advected past each other before having had enough time to develop stickers. As a consequence, the contribution of the corresponding nonequilibrium sticker forces to the stress becomes constant, independent of the particular shear rate. The viscosity then drops proportional to $\dot{\gamma}^{-1}$ until the thermodynamic forces take over. In this section, we study elongational flow in a similar way.

In this paper, we concentrate on planar elongational flow characterized by

$$\mathbf{V}(\mathbf{r}) = \begin{pmatrix} \dot{\epsilon} & 0 & 0 \\ 0 & -\dot{\epsilon} & 0 \\ 0 & 0 & 0 \end{pmatrix} \cdot \mathbf{r} \quad (5)$$

In particle based simulations, it can be implemented in a continuous way using a method proposed by Todd and Daivis^[25,26] and by Baranyai and Cummings.^[27] Both methods are based on work of Kraynik and Reinelt.^[28] The basic idea is to perform a checkerboard simulation with $\langle \mathbf{V}(\mathbf{r}) \rangle$ in Equation (1) replaced by $\mathbf{V}(\mathbf{r})$ according to Equation (5) above. The central box, i.e. the unit cell of the checkerboard, is chosen such that after a finite simulation time τ_p the deformed box coincides with some unit cell of the lattice generated by the original box. At this time, all particles are mapped to the original unit cell and the run is continued. Some details are presented in Appendix B.

The elongational viscosity is usually defined by

$$\tilde{\eta}_{\text{elo}} = \frac{S_{xx} - S_{yy}}{\dot{\epsilon}} \quad (6)$$

In the case of a Newtonian liquid, this results in $\tilde{\eta}_{\text{elo}} = 4\eta$, with η the shear viscosity. The factor of 4 is called

the Trouton factor for this particular case. It is natural to define the planar elongational viscosity η_{elo} by $\eta_{\text{elo}} = \tilde{\eta}_{\text{elo}}/4$. With this definition, a unified expression for the viscosity, holding both for shear flow and for elongational flow,^[29] reads

$$\eta = \frac{\mathbf{S} : \mathbf{D}}{\mathbf{D} : \mathbf{D}} = \frac{\mathbf{S} : \mathbf{D}}{I_2} \quad (7)$$

where $\mathbf{D} = [\nabla \mathbf{u} + (\nabla \mathbf{u})^T]$ is the rate of deformation tensor. The latter definition basically says that the rate of dissipation $\frac{1}{2} \mathbf{S} : \mathbf{D}$ is proportional to $\frac{1}{2} \mathbf{D} : \mathbf{D}$, with constant of proportionality equal to η .

In Figure 6 (upper panel), we have plotted $\tilde{\eta}_{\text{elo}}$, η_{elo} and η as a function of $\dot{\epsilon}$ and $\dot{\gamma}$, respectively for the system defined

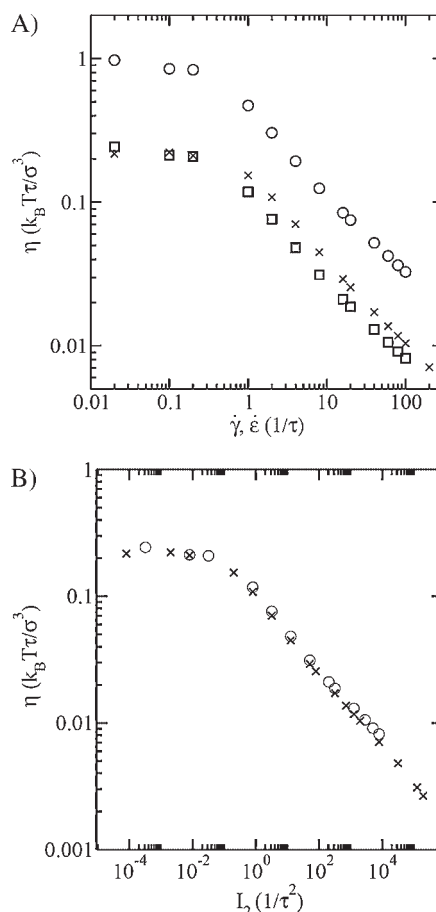


Figure 6. Upper panel shows the viscosity versus the deformation rate. The circles depict the viscosity measured under elongation flow via $\tilde{\eta}_{\text{elo}} = (S_{xx} - S_{yy})/\dot{\epsilon}$, whereas the squares represent the elongational viscosity including the Trouton factor, i.e. $\eta_{\text{elo}} = \tilde{\eta}_{\text{elo}}/4$. The viscosity measured from $\eta = S_{xy}/\dot{\gamma}$ under simple linear shear is given by the crosses. The lower panel shows the generalized viscosity as a function of the second scalar invariant of the deformation tensor I_2 for shear (crosses) and elongation flow (circles). The second scalar invariant I_2 is defined as $2\dot{\gamma}^2$ and $8\dot{\epsilon}^2$ for shear and elongation flow, respectively.

in Table 1. It is interesting to notice that just like in the case of a Newtonian liquid, after correcting for the Trouton factor, the elongational viscosity at low deformation rates becomes equal to the shear viscosity. At higher $\dot{\epsilon}$ and $\dot{\gamma}$, both viscosities behave qualitatively similarly, but start deviating quantitatively. Equation (7) above, however, suggests that we plot both viscosities as a function of $I_2 = \mathbf{D}:\mathbf{D}$, i.e. as a function of $2\dot{\gamma}^2$ in the case of shear flow and $8\dot{\epsilon}^2$ in the case of elongational flow. This is done in Figure 6 (lower panel). Somewhat to our surprise, may be, both curves now agree very well over several decades of I_2 . This suggests that as far as dissipation is concerned, shear flow and elongational flow are very similar. Only at the higher values of I_2 , very small deviations between the two curves are discernible.

Superposition Rheology

In this section, we investigate the possible anisotropic rheological properties of the fluid induced by the applied shear flow. To this end, we calculate the resistance of the fluid to a shearing motion perpendicular to the applied shear flow. To be more precise, we apply a shear flow in the x -direction with gradient along the y -direction and then perturb the system with a force on each particle i given by

$$\mathbf{f}_i = f_0 \cos(ky_i) \hat{\mathbf{e}}_z \quad (8)$$

where y_i is the y -coordinate of particle i and $\hat{\mathbf{e}}_z$ is the unit vector in the z -direction. This force will produce an additional flow field

$$\mathbf{v}(\mathbf{r}) = \frac{\rho f_0}{k^2 \eta_{\perp}} \cos(ky) \hat{\mathbf{e}}_z \quad (9)$$

where ρ is the mass density and η_{\perp} is the viscosity for this particular type of flow; y is the y -coordinate of \mathbf{r} . Inverting this equation we obtain

$$\begin{aligned} \frac{\rho f_0}{k^2 \eta_{\perp}} &= \frac{2}{L^3} \int d^3 \mathbf{r} \cos(ky) \mathbf{v}(\mathbf{r}) \cdot \hat{\mathbf{e}}_z \\ &= \frac{2}{N} \left\langle \sum_{i=1}^N v_{iz} \cos(ky_i) \right\rangle \end{aligned} \quad (10)$$

where the angular brackets indicate a time averaging. We have used this result to calculate η_{\perp} . The velocity needed to do so was calculated from $d\mathbf{r}_i = \mathbf{v}_i dt$, with $d\mathbf{r}_i$ from Equation (1).

We performed simulations using $k = 2\pi/L$ and either $f_0 = 0.0242k_B T/\sigma$ or $f_0 = 0.0024k_B T/\sigma$, and found reasonable agreement between both cases. Even smaller values of f_0 did not change the results. The value of η_{\perp} for $\dot{\gamma} = 0$ is shown on the vertical axis in Figure 7 and agrees very well

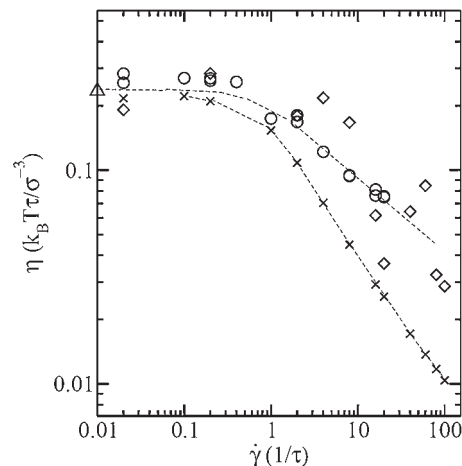


Figure 7. The viscosity η measured from the stress tensor under simple shear (crosses) and via the superposition of external forces η_{\perp} (circle and diamond). The amplitude of the external force was $0.0242k_B T/\sigma$ (circles) and $0.0024k_B T/\sigma$ (diamonds), where the force was directed in the z -direction with a gradient in the y -direction perpendicular to the shear flow. The triangle at the vertical axis represents η_{\perp} measured at zero shear.

with η obtained from standard nonequilibrium simulations. This proves that both values of f_0 are small enough to obtain reliable results, and, incidentally, that including sticker forces when calculating the stress tensor is the right thing to do. Finally, we checked that the values of S_{xy} in the perturbed case are equal to those in the unperturbed case.

In Figure 7, we have plotted both η_{\perp} and η as a function of $\dot{\gamma}$. It is seen that for values of $\dot{\gamma}$ smaller than about $1/\tau$ both types of viscosity agree very well, indicating that the shear flow has not substantially changed the structure of the liquid. For shear rates equal to $1/\tau$ or larger both curves start to deviate. This is somewhat surprising, since for both types of flow, i.e. the applied shear flow and the flow resulting from the applied perturbation, the gradient direction is the same. Restructuring induced by the applied shear flow is expected to affect mainly the correlations along the gradient direction leaving unchanged the structure within the vorticity plane. Still it appears that forces along different directions in the vorticity plane are different. One explanation for this may be that at these very large shear rates the structure of the particles in the layers parallel to the vorticity plane becomes anisotropic in an effort to minimize dissipation.

Shear Banding

In a recent paper, we described the occurrence of shear banding in a system with parameters given in Table 1, except for the value of α , which was set equal to $5.1k_B T$. Depending on the initial configuration, the system would split into several bands, stacked along the gradient

direction. When run long enough, all systems finally settled in a banded state of just two bands, one high shear rate band and one low shear rate band. An extended study of this system is presented in Figure 8. In Figure 8 (upper panel), we have plotted the maximum and minimum shear rates, measured in boxes in their final stationary states, as a function of applied shear rate and for a wide range of values of the sticker parameter α . In Figure 8 (lower panel) the same has been done for the densities. From these figures, we infer that for values of α larger than about $4.0k_B T$ all systems shear band in some range of imposed shear rates. Outside these ranges, the systems behave normally, i.e. develop linear flow fields with shear rates equal to the imposed shear rates. With increasing α , the density in the high shear rate band becomes smaller. Eventually, the high shear rate band is very narrow, has a very high shear rate and a very low density, and so has all the characteristics of a crack.

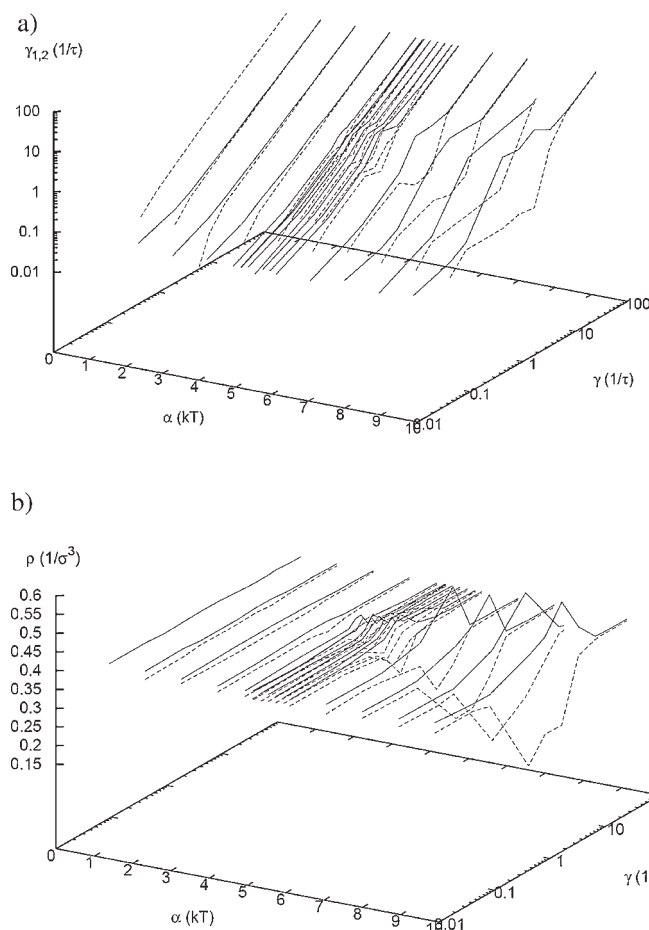


Figure 8. Maximum and minimum shear rates $\dot{\gamma}_{1,2}$ (upper panel) and maximum and minimum number densities ρ (lower panel) as a function of the overall imposed shear rate $\dot{\gamma}$ and strength of the sticker forces α . Shear banding is observed for $\alpha > 4.0k_B T$, as the maximum and minimum shear rates start to deviate from the imposed shear rate.

In this section, we will first study the influence of using stick boundary conditions on the flow profiles instead of the periodic boundary conditions used so far. We will study the same system as before, i.e. the one characterized by Table 1 except for the value of α , which is taken to be $5.1k_B T$. We then change the density in the system to half of its original value and study the time development of the emerging bands after start up of shear.

Stick Boundary Conditions

In our previous work, we found that at imposed shear rates slightly beyond those where shear banding occurred, stresses were still decreasing with increase in imposed shear rates. We attributed this behaviour to the finite sizes of our systems and possibly to the use of periodic boundary conditions. Whereas with periodic boundary conditions, the 'interface' between the two bands may occur anywhere in the box, with stick boundary conditions its position is dictated by the moving boundaries. In Figure 9, we have plotted average velocities as a function of the position along the gradient direction as they were measured in the box, i.e. without shifting the profile along the gradient direction. Indeed it is seen that the high shear rate bands occur in the upper part of the box and the low shear rate bands in the lower part. In all cases, the 'interfaces' are quite narrow and the shear rates in both bands are well defined. As a result, the positions of the interfaces are fixed by the lever rule

$$\dot{\gamma} = f \dot{\gamma}_1 + (1 - f) \dot{\gamma}_2 \quad (11)$$

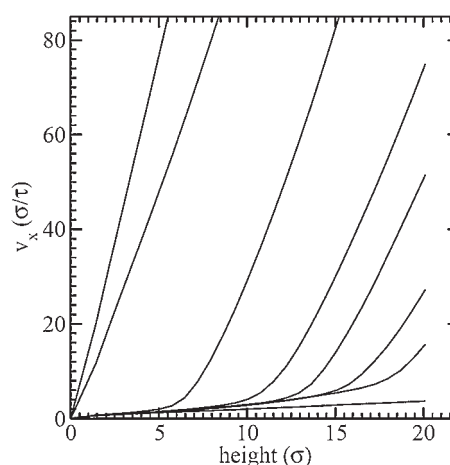


Figure 9. Velocity in the shear direction v_x as a function of the box height. The imposed shear rate is (from bottom to top): 0.2, 1.0, 1.6, 2.8, 4.0, 8.0, 12.0 and 16.0 τ^{-1} . Stick, nonperiodic boundary conditions were applied at the top and bottom of the simulation box. The top wall moves in the x -direction at a speed of $\dot{\gamma}L_y$, while the bottom was fixed.

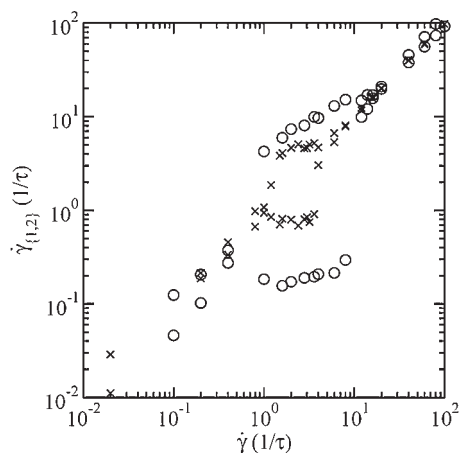


Figure 10. The local shear rate of the high and low shear bands $\dot{\gamma}_{1,2}$ versus the imposed shear rate $\dot{\gamma}$ for $\alpha = 5.1kT$. Results from the periodic boundary conditions are represented by crosses, the shear rates measured in the stick boundary conditions simulations are given by the circles.

where f denotes the fraction of the box occurring in the low shear rate band.

In Figure 10, we have plotted the shear rates in the two bands as a function of the imposed shear rate, both for the present box with stick boundary conditions (circles) and for the box with periodic boundary conditions described previously (crosses). Two differences between these two cases are immediate. First, the shear rates in the two bands are more extreme in the stick boundary case than in the periodic boundary case, i.e. the low shear rates are smaller in the stick boundary case than in the periodic boundary case and the high shear rates are larger. Moreover, the range of imposed shear rates where shear banding occurs is somewhat larger in the stick boundary case than in the periodic boundary case, extending to larger values of imposed shear rates.

In Figure 11, we have plotted the stresses in both cases as a function of the imposed shear rates. At those shear rates where no shear banding occurs, stresses are marginally smaller in the boxes with stick boundary conditions compared to those in the boxes with periodic boundary conditions. This may probably be due to the fact that the stick boundary condition effectively reduces the volume of the box a bit. The volume occurring in the denominator of the expression for the stress is therefore actually a bit smaller than the nominal volume of the box used in our calculations. The regions where shear banding occurs are indicated by dashed boxes in both cases. Again, it is obvious that in the case of stick boundary conditions the range of shear rates over which banding occurs is larger than in the case of periodic boundary conditions. Second, while in the case of periodic boundary conditions, stresses were decaying at imposed shear rates slightly above the

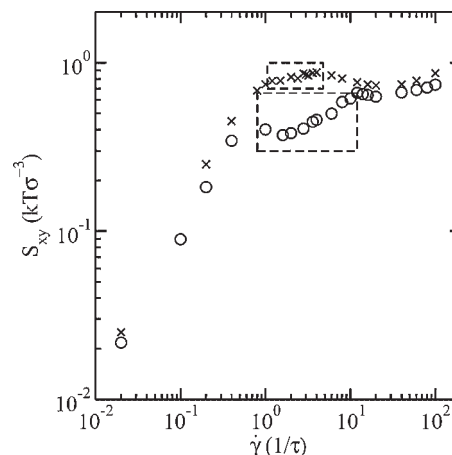


Figure 11. Shear stress S_{xy} in flow direction as a function of the shear rate $\dot{\gamma}$ for $\alpha = 5.1kT$. Results from the periodic boundary conditions are represented by crosses, the stress measured in the stick boundary conditions simulations are given by the circles. The dashed boxes indicate the imposed shear rates where shear bands are observed.

banding regime, this does not occur with stick boundary conditions. On the other hand, with stick boundary conditions, a slight decrease of the stress occurs in the banding regime at low shear rates. A third interesting point to be mentioned concerns the growth of stresses with imposed shear rates in the (major part of the) banding regime. It is clearly seen that in the banding regime, with increasing shear rates, stresses increase according to a power law with exponent close to 0.3. This is in very good agreement with experimental findings by Berret et al.^[1]

Time Evolution of the Bands After Start up of Shear

Finally, we study the evolution of bands emerging after start up of shear, and how they finally settle in a stationary state. In order to make possible the occurrence of multibanded states, it is advantageous to use boxes which are substantially larger along the gradient direction than the one used until now. We, therefore, set the box dimension along the gradient direction, i.e. the height of the box, equal to 43σ . At the same time, in order to keep CPU times as short as possible, we change the volume fraction of hard material from 0.2 to 0.1. With a value of $\alpha = 9.5k_B T$ we obtain multiply banded states, well suited for visual inspection and stress calculations. In all the cases described in this section, the shear rate was equal to $7.5(1/\tau)$.

In Figure 12, we have plotted the evolution of the average velocity field in a system starting with a linear velocity profile at time zero. In the top panel, every line represents the average velocity in a slab at a height proportional to the number of the line, counted from the bottom of the figure. The width of each slab was 0.72σ . It is

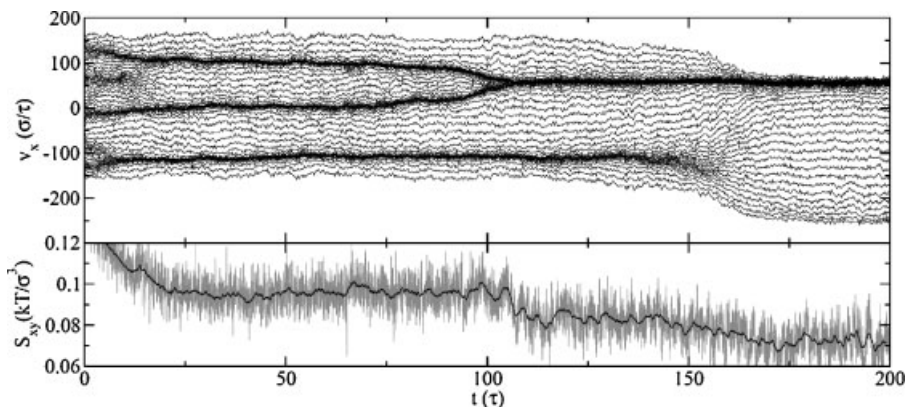


Figure 12. Time evolution of the velocity profile (top) and corresponding stress (bottom). Every line in the top figure represents the velocity at evenly distributed heights in the simulation box: little separation between lines corresponds to low shear rate bands. The initial velocity profile was linear with an imposed shear rate of $7.5(1/\tau)$. Eventually, the system separates in one high and one low shear rate band by merging several bands. At the bottom, we plot the corresponding stress (grey) and a running average over blocks of 100 data points (black).

clearly seen that after start up the system quickly splits into several bands. Bands with widely separated lines are high shear rate bands, those with little or no separation between the lines are low shear rate bands. At the very early stages, five low shear rate bands and five high shear rate bands may be discerned. After some quick rearrangements, from time 15τ on, the system temporarily settles in a quasi-stationary state, with three bands of each type. At time about 100τ two low shear rate bands merge into one. This may also be expressed by saying that a high shear rate band between two low shear rate bands ceases to exist. So after this process, two bands, one of each type, have

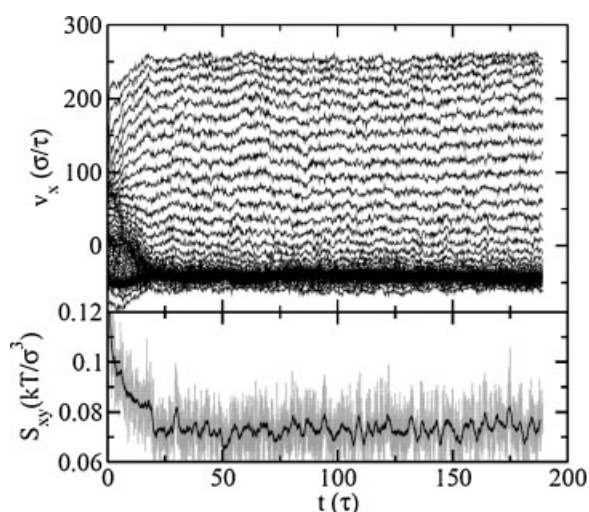


Figure 13. The time evolution of the velocity profile and stress for a simulation of an initially banded velocity profile, plotted in the same way as Figure 12. The overall imposed shear rate equals $7.5(1/\tau)$.

disappeared and we are left with four bands, two of each type. At time 150τ two more bands disappear, after which the system settles in its final state, consisting of one low shear rate band and one high shear rate band. An apparent drift of all velocities seems to take place concomitantly with this last event. The explanation for this comes from the fact that during all runs we kept the total momentum equal to zero. Since the density in the high shear rate band is very low compared to that in the low shear rate band, the distribution of the velocities is necessarily skew.

In the upper panel of Figure 13, flow profiles are sketched for a

similar system, but now prepared in a banded state at time zero. After some vague banding at early times, but mainly some substantial redistribution of mass, quickly the final stationary state appears at about $t = 20\tau$.

In the lower panels of Figure 12 and 13, we have plotted the stress development with the evolution of the velocity in the corresponding upper panel. In both cases, the stress decays quickly in order to settle at some stationary or quasi-stationary value. In the latter case, with every major event bringing the system from one quasi-stationary state to the next, the stress diminishes substantially. This process continues till the final stationary state is selected such that the stress is minimal. Since in every (quasi) stationary state the stress is constant throughout the system, the volume-averaged stress discussed so far is proportional to the rate of dissipation

$$W = \int dV \nabla \cdot (S \cdot \mathbf{u}) \quad (12)$$

We, therefore, hypothesize that the final stationary state, whether banded or not, is selected on the basis of minimal overall dissipation. Obviously, the local dissipation does not have to be constant throughout the system.

Summary

We have discussed results of simulations of a particular model of core-shell particles. Each particle of our model consists of a hard core to which a thick and soft corona is attached. The hard core and the corona together give rise to interactions between the particles described by a soft potential of mean force ϕ . Besides these interactions, to

each pair of particles a number n_{ij} is attributed, which describes the thermodynamic state of the overlapping coronas. Temporary deviations of the sticker numbers from their equilibrium values give rise to transient forces, which contribute substantially to the rheological properties of the system. Since frictions are large, or in other words characteristic times are long, the propagator of choice is a first order Brownian propagator. In Appendix A, we describe a Gallilei invariant second-order Langevin propagator, which may be of use in similar systems with smaller frictions.

In the section Elongational viscosities, we have found that elongational viscosities, provided the Trouton factor is included in their definition and they are plotted against $8\dot{\epsilon}^2$, coincide with shear viscosities plotted against $2\dot{\gamma}^2$. Note that the same should hold when plotted against $2\dot{\epsilon}$ and $\dot{\gamma}$, respectively. Once we realize that simple shear flow is composed of a rotation and a planar elongation with elongation rate equal to $\frac{1}{2}\dot{\gamma}$ these findings are obvious.

In the section Superposition rheology, we studied the response of a sheared system to a perturbation causing a flow along the main vorticity direction with gradient along the main gradient direction. From the results, we inferred that at high shear rates the particles gather together in planes perpendicular to the gradient direction and that at very high shear rates these planes are slightly anisotropic. It will be interesting to extend these studies in order to provide guidance to the interpretation of future experiments in superposition rheology.

In the final section, we found that with a suitable choice of the sticker force strength α , the system could be made to shear band in a well-defined regime of shear rates. α should be chosen such that the sticker forces yield the dominant contribution to the stress tensor. Shear banding then occurs around values of $\dot{\gamma}$ where sticker forces become constant or even decrease with shear rate. In rate controlled simulations using stick boundary conditions, stresses in the banded regime are selected proportional to $\dot{\gamma}^{0.3}$, in good agreement with experiments on worm-like micelles. We hypothesize that banding of the system occurs in an effort to minimize dissipation.

Finally, let us mention that the model, used in this paper, not only applies to core-shell particles or star polymer but also with small adjustments can be used to simulate other systems, like for example polymer melts and solutions or block copolymers.

Appendix A: Second Order Model

In this appendix, we present a set of second order equations of motion for our model. In order to do so, we associate a mass μ and velocity v_{nij} with every sticker number n_{ij} . We take the probability distribution that we

want to sample at equilibrium to be given by

$$P_{eq} \propto \exp \left\{ -\beta \sum_i \frac{1}{2} m \mathbf{v}_i^2 + \sum_{\langle ij \rangle} \left[\phi(r_{ij}) + \frac{1}{2} \mu v_{nij}^2 + \frac{1}{2} \alpha (n_{ij} - n_0(r_{ij}))^2 \right] \right\}, \quad (A1)$$

where m is the mass and \mathbf{v}_i is the velocity of the particle i . The standard procedure to derive the Fokker-Planck equations admitting this distribution as its stationary state^[30–32] then leads to the following equation of motion:

$$m \frac{d\mathbf{v}_i}{dt} = \sum_j \left\{ -\nabla_i \phi(r_{ij}) + \alpha [n_{ij} - n_0(r_{ij})] \frac{dn_0}{dr_{ij}} \frac{\mathbf{r}_{ij}}{r_{ij}} \right\} + \mathbf{f}_i^F + \mathbf{f}_i^R$$

$$\mu \frac{dv_{nij}}{dt} = -\alpha [n_{ij} - n_0(r_{ij})] + f_{nij}^F + f_{nij}^R \quad (A2)$$

where \mathbf{f}_i^F and \mathbf{f}_i^R are the friction and random force acting on particle i , and f_{nij}^F and f_{nij}^R are the friction and random force acting on sticker number n_{ij} . In both cases, the friction and random forces are related by the fluctuation-dissipation theorem, to be discussed next.

We start with \mathbf{f}_i^F and \mathbf{f}_i^R . Among the many possible choices for the friction force \mathbf{f}_i^F , there is one outstanding choice, first introduced by Hoogerbrugge and Koelman in their well-known DPD model.^[33,34] In accordance with their model, we choose \mathbf{f}_i^F to be a sum of pair frictions proportional to $\mathbf{v}_{ij} \cdot \hat{r}_{ij} \hat{r}_{ij}$, when $\mathbf{v}_{ij} = \mathbf{v}_i - \mathbf{v}_j$ and \hat{r}_{ij} is a unit vector in the direction of $\mathbf{r}_i - \mathbf{r}_j$. The reason for the particular usefulness of this type of friction forces is that they are Gallilean invariant, and therefore can be used to simulate systems in flow. Once the friction forces are defined, the random forces are dictated^[35] by the fluctuation-dissipation theorem:

$$\mathbf{f}_i^F = - \sum_j \tilde{\xi}(n_{ij}) \mathbf{v}_{ij} \cdot \hat{r}_{ij} \hat{r}_{ij}$$

$$\mathbf{f}_i^R = \sum_j \sqrt{2k_B T \tilde{\xi}(n_{ij}) / dt} \theta \hat{r}_{ij} \quad (A3)$$

where dt is the time step and θ is a random number with zero mean and unit variance. We have added a tilde in the friction constant $\tilde{\xi}(n_{ij})$ in order to discriminate it from the friction used in the main text. Similarly to what was done in the main text, we take $\tilde{\xi}(n_{ij})$ to be given by

$$\tilde{\xi}(n_{ij}) = \tilde{\xi}_s \frac{1}{2} (n_{ij} + |n_{ij}|) n_0(r_{ij}) + \tilde{\xi}_0 \quad (A4)$$

We choose $n_0(r_{ij})$ to be the same as in the main text.

Similarly, we take f_{nij}^F proportional to $-v_{nij}$ and find f_{nij}^R from the fluctuation–dissipation theorem:

$$\begin{aligned} f_{nij}^F &= -\alpha\tau v_{nij} \\ f_{nij}^R &= \sqrt{2k_B T \frac{d\tau}{dt}} \theta \end{aligned} \quad (\text{A5})$$

We have written the constant of proportionality in f_{nij}^F as $\alpha\tau$, in order to emphasize the role of τ as a characteristic time. This can be understood by going back to the equation of motion for n_{ij} , but now omitting the random term:

$$\mu \frac{dv_{nij}}{dt} = -\alpha[n_{ij} - n_0(r_{ij})] - \alpha\tau v_{nij} \quad (\text{A6})$$

This equation describes the time evolution of a damped harmonic oscillator. In case μ is chosen smaller than $\alpha\tau^2/4$, n_{ij} will exponentially approach $n_0(r_{ij})$ with characteristic time τ .

We end this appendix with a short test of the second order model just described. Typical masses of the core-shell particles are in the range of $1.2 \times 10^9 \text{ g}\cdot\text{mol}^{-1}$. To prove that the fluctuation–dissipation theorem has been applied correctly, we measured the temperature in three different ways. Since the probability distribution at equilibrium has three independent Gaussian factors, pertaining to the velocities \mathbf{v} of the particles, the velocities v_{nij} of the sticker numbers, and the harmonic potential for the number of stickers ($n_{ij} - n_0$), we can calculate

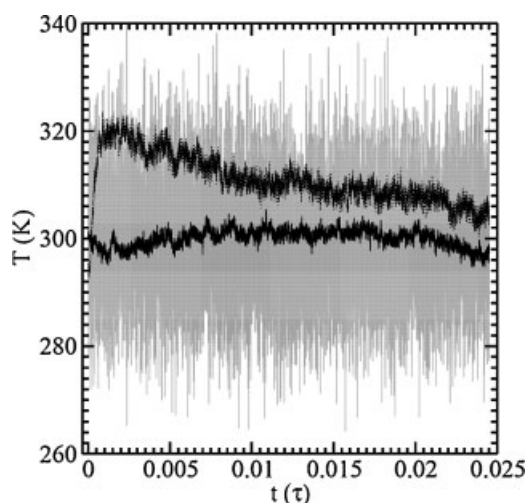


Figure 14. Instantaneous temperature for second order model based on particle velocity (v ; grey), rate of change for number of stickers (v_{nij} ; solid line) and fluctuations of number of stickers ($(n_{ij} - n_0)$; dotted). Both kinetic terms fluctuate around the imposed temperature (300 K), while the temperature based on the fluctuations in the number of stickers slowly decays to the imposed temperature.

temperatures based on these three sets of degrees of freedom. In Figure 14, we plot the actual temperature during the simulation for the three terms. The temperature based on the particle velocity and rate of change of the number of stickers both fluctuate around the imposed temperature of 300 K. The instantaneous temperature based on the fluctuations in the number of stickers deviates from the imposed temperature at the start of the run and slowly decays to the imposed temperature. Note that the simulation time is merely a fraction of τ , which takes 3 weeks of CPU time in this simulation.

Appendix B: Continuous Planar Elongational Flow Boundary Conditions

Since we restrict ourselves to planar elongational flow, we can leave one axis out of our considerations. For convenience, we let the two elongational axes be the x -axis and the y -axis and assume that the periodic box initially has unit vectors $\mathbf{b}_1 = (\cos\theta, \sin\theta)^T$ and $\mathbf{b}_2 = (-\sin\theta, \cos\theta)^T$. From an integration of Equation (5), we find that after a time t these vectors have developed into $\mathbf{b}_1(t) = (\lambda \cos\theta, \lambda^{-1} \sin\theta)^T$ and $\mathbf{b}_2(t) = (-\lambda \sin\theta, \lambda^{-1} \cos\theta)^T$ with $\lambda = \exp(\dot{\epsilon}t)$. By adjusting θ we make sure that after some time $t = \tau_p$, the new vectors coincide with two lattice vectors generated by the original unit cell:

$$\mathbf{b}_1(\tau_p) = N_{11}\mathbf{b}_1 + N_{12}\mathbf{b}_2$$

$$\mathbf{b}_2(\tau_p) = N_{21}\mathbf{b}_1 + N_{22}\mathbf{b}_2$$

where N_{ij} are integers. Solving for N_{ij} we find

$$N_{11} = \lambda_p - (\lambda_p - \lambda_p^{-1}) \sin^2 \theta$$

$$N_{12} = N_{21} = -(\lambda_p - \lambda_p^{-1}) \sin \theta \cos \theta$$

$$N_{22} = \lambda_p^{-1} + (\lambda_p - \lambda_p^{-1}) \sin^2 \theta$$

Once a set of N_{ij} found by solving these equations, θ follows from

$$\tan \theta = \frac{\sin^2 \theta}{\sin \theta \cos \theta} = \frac{N_{11} - \lambda_p}{N_{12}}$$

$$\lambda_p + \lambda_p^{-1} = N_{11} + N_{22}$$

Among the many solutions found by Kraynik and Reinelt one is given by $N_{11} = 2$, $N_{12} = -1$ and $N_{22} = 1$. θ and $\tau_p = \dot{\epsilon}^{-1} \ln \lambda_p$ then follow from the last two equations.

Acknowledgements: This work is supported with a grant of the Dutch Programme EET (Economy, Ecology, Technology), a joint initiative of the Ministeries of Economic Affairs, Education, Culture and Sciences and of Housing, Spatial Planning and the Environment. We thank P. Kindt for many illuminating discussions.

Received: May 3, 2007; Revised: August 29, 2007; Accepted:
August 30, 2007; DOI: 10.1002/mats.200700029

Keywords: core-shell polymers; resins; rheology; simulations

- [1] J. F. Berret, D. C. Roux, G. Porte, P. Lindner, *Europhys. Lett.* **1994**, 25, 521.
- [2] J. B. Salmon, A. Colin, S. Manneville, F. Molino, *Phys. Rev. Lett.* **2003**, 90, 228303.
- [3] J. B. Salmon, S. Manneville, A. Colin, *Phys. Rev. E* **2003**, 68, 051503.
- [4] S. Manneville, J. B. Salmon, L. Becu, A. Colin, F. Molino, *Rheol. Acta* **2004**, 43, 408.
- [5] J. P. Decruppe, S. Lerouge, J. F. Berret, *Phys. Rev. E* **2001**, 63, 022501.
- [6] S. Lerouge, J. P. Decruppe, J. F. Berret, *Langmuir* **2000**, 16, 6464.
- [7] P. Tapadia, S. Ravindranath, S. Q. Wang, *Phys. Rev. Lett.* **2006**, 96, 196001.
- [8] P. Tapadia, S. Q. Wang, *Phys. Rev. Lett.* **2006**, 96, 016001.
- [9] W. M. Holmes, P. T. Callaghan, D. Vlassopoulos, J. Roovers, *J. Rheol.* **2004**, 48, 1085.
- [10] D. Vlassopoulos, G. Fytas, T. Pakula, J. Roovers, *J. Phys. Condens. Matter* **2001**, 13, R855.
- [11] P. Fisher, *Rheol. Acta* **2000**, 39, 234.
- [12] P. Fisher, E. K. Wheeler, G. G. Fuller, *Rheol. Acta* **2002**, 41, 35.
- [13] N. A. Spenley, M. E. Cates, T. C. B. McLeish, *Phys. Rev. Lett.* **1993**, 71, 939.
- [14] J. K. G. Dhont, *Phys. Rev. E* **1999**, 60, 4534.
- [15] P. D. Olmsted, P. M. Goldbart, *Phys. Rev. A* **1992**, 46, 4966.
- [16] P. D. Olmsted, O. Radulescu, C. Y. D. Lu, *J. Rheol.* **2000**, 44, 257.
- [17] S. M. Fielding, P. D. Olmsted, *Phys. Rev. E* **2003**, 68, 036313.
- [18] S. M. Fielding, P. D. Olmsted, *Euro. Phys. J. E* **2003**, 11, 65.
- [19] S. M. Fielding, P. D. Olmsted, *Phys. Rev. Lett.* **2006**, 96, 104502.
- [20] A. van den Noort, W. K. den Otter, W. J. Briels, *Europhys. Lett.* **2007**, 80, 28003.
- [21] A. van den Noort, W. J. Briels, 2007, submitted.
- [22] D. E. Grady, *Mech. Mat.* **1994**, 17, 289.
- [23] M. P. Allen, D. J. Tildesley, "Computer Simulation of Liquids", Clarendon, Oxford 1987.
- [24] M. Kröger, S. Hess, *Phys. Rev. Lett.* **2000**, 85, 1128.
- [25] B. D. Todd, P. J. Daivis, *Phys. Rev. Lett.* **1998**, 81, 1118.
- [26] M. L. Matin, P. J. Daivis, B. D. Todd, *J. Chem. Phys.* **2000**, 113, 9122.
- [27] A. Baranyai, P. T. Cummings, *J. Chem. Phys.* **1999**, 110, 42.
- [28] A. M. Kraynik, D. A. Reinelt, *Int. J. Multiphase Flow* **1992**, 18, 1045.
- [29] M. N. Hounkonnou, C. Pierleoni, J. P. Ryckaert, *J. Chem. Phys.* **1992**, 97, 9335.
- [30] C. W. Gardiner, "Handbook of Stochastic Methods", Springer, Berlin 1985.
- [31] P. Espanol, *Phys. Rev. E* **1995**, 52, 1734.
- [32] W. J. Briels, "Theory of Polymer Dynamics", Lecture notes, Uppsala University, 1994.
- [33] P. J. Hoogerbrugge, J. M. V. A. Koelman, *Europhys. Lett.* **1992**, 19, 155.
- [34] J. M. V. A. Koelman, P. J. Hoogerbrugge, *Europhys. Lett.* **1993**, 21, 363.
- [35] P. Espanol, P. Warren, *Europhys. Lett.* **1995**, 30, 191.